Inorganic Chemistry

Article

pubs.acs.org/IC

Phosphide Oxides RE_2AuP_2O (RE = La, Ce, Pr, Nd): Synthesis, Structure, Chemical Bonding, Magnetism, and ^{31}P and ^{139}La Solid State NMR

Timo Bartsch,[†] Thomas Wiegand,[‡] Jinjun Ren,[‡] Hellmut Eckert,[‡] Dirk Johrendt,[§] Oliver Niehaus,[†] Matthias Eul,[†] and Rainer Pöttgen*[,†]

[†]Institut für Anorganische und Analytische Chemie, Universität Münster, Corrensstrasse 30, 48149 Münster, Germany

[‡]Institut für Physikalische Chemie, Universität Münster, Corrensstrasse 30, 48149 Münster, Germany

[§]Department Chemie, Ludwig-Maximilians-Universität München, Butenandtstrasse 5-13, 81377 München, Germany

Supporting Information

ABSTRACT: Polycrystalline samples of the phosphide oxides RE_2AuP_2O (RE = La, Ce, Pr, Nd) were obtained from mixtures of the rare earth elements, binary rare earth oxides, gold powder, and red phosphorus in sealed silica tubes. Small single crystals were grown in NaCl/KCl fluxes. The samples were studied by powder X-ray diffraction, and the structures were refined from single crystal diffractometer data: La_2AuP_2O type, space group $C2/m$, a = 1515.2(4), b = 424.63(8), c = 999.2(2) pm, β = 130.90(2)°, wR2 = 0.0410, 1050 F^2 values for Ce_2AuP_2O, and a = 1503.6(4), b = 422.77(8), c = 993.0(2) pm, β = 130.88(2)°, wR2 = 0.0401, 1037 F^2 values for Pr_2AuP_2O, and a = 1501.87(5), b = 420.85(5), c = 990.3(3) pm, β = 131.12(1)°, wR2 = 0.0944, 1143 F^2 values for Nd_2AuP_2O with 38 variables per refinement. The structures are composed of $[RE_2O]^{4+}$ polycationic chains of *cis*-edge-sharing $ORE_{4/2}$ tetrahedra and polyanionic strands $[AuP_2]^{4-}$, which contain gold in almost trigonal–planar phosphorus coordination by P^{3-} and P_2^{4-} entities. The isolated phosphorus atoms and the P_2 pairs in La_2AuP_2O could clearly be distinguished by ^{31}P solid state NMR spectroscopy and assigned on the basis of a double quantum NMR technique. Also, the two crystallographically inequivalent La sites could be distinguished by static ^{139}La NMR in conjunction with theoretical electric field gradient calculations. Temperature-dependent magnetic susceptibility measurements show diamagnetic behavior for La_2AuP_2O. Ce_2AuP_2O and Pr_2AuP_2O are Curie–Weiss paramagnets with experimental magnetic moments of 2.35 and 3.48 μ_B per rare earth atom, respectively. Their solid state ^{31}P MAS NMR spectra are strongly influenced by paramagnetic interactions. Ce_2AuP_2O orders antiferromagnetically at 13.1(5) K and shows a metamagnetic transition at 11.5 kOe. Pr_2AuP_2O orders ferromagnetically at 7.0 K.

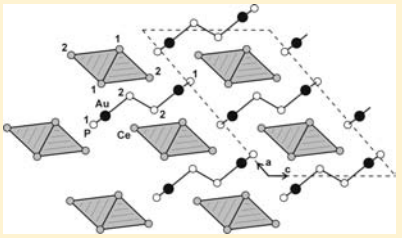

INTRODUCTION

The large field of iron pnictide and pnictide oxide chemistry comprises numerous spin-density wave and high-temperature superconducting compounds, outstanding examples of which are $ThCr_2Si_2$ type $BaFe_2As_2$[1−3] and ZrCuSiAs type LaFeAsO.[4,5] Striking structural motifs of these materials are layers of edge-sharing $FePn_{4/4}$ tetrahedra, which in the case of $BaFe_2As_2$ are stacked in an AA′AA′ sequence (A′ being the mirror image of A), leaving large Fe_8As_8 cavities for the barium atoms. The LaFeAsO structure contains a second layer type. The oxygen atoms are surrounded tetrahedrally by four La atoms, and these La_4 tetrahedra are condensed via common edges. The $FeAs_{4/4}$ and $OLa_{4/4}$ layers are stacked in an ABAB sequence. The charge spin-density wave in $BaFe_2As_2$ and LaFeAsO can be suppressed by diverse doping experiments, leading to the onset of superconductivity. The structure–property relationships of the many investigated phases have been reviewed.[6−21]

The critical temperature of the superconducting phases can be tuned by changing the distance between the iron pnictide layers. Besides simple substitution experiments with larger atoms, many phases with larger oxidic blocks have been synthesized. An overview is given in refs 9, 14, and 20. Apart from the oxidic separating blocks, it is also possible to introduce halide slabs as recently observed for $La_5Cu_4As_4O_4Cl_2$.[22] Although these compounds crystallize with different structure types, their common motif is a layer-like stacking of pnictide and oxide slabs.

The recently discovered La_2AuP_2O[23] reflects a new structural aspect of pnictide oxide chemistry with regard to the dimensionality of the building units. This quaternary compound is composed of polymeric chains $[La_2O]^{4+}$ of *cis*-edge-sharing $OLa_{4/2}$ tetrahedra and strands of $[AuP_2]^{4-}$ polyanions. As part of our investigations on structure–property relationships of pnictide oxides, the present study reports the crystal and electronic structures of the magnetic isotypic compounds RE_2AuP_2O (RE = Ce, Pr, and Nd) as well as a detailed ^{31}P solid state NMR spectroscopic study of La_2AuP_2O.

Received: November 15, 2012
Published: February 1, 2013

   dx.doi.org/10.1021/ic302475u | *Inorg. Chem.* 2013, 52, 2094−2102

Table 1. Lattice Parameters of RE_2AuP_2O

compound	a (pm)	b (pm)	c (pm)	β (deg)	V (nm^3)
La_2AuP_2O[a]	1537.3(3)	427.39(8)	1009.2(2)	131.02(1)	0.5003
Ce_2AuP_2O	1515.2(4)	424.63(8)	999.2(2)	130.90(2)	0.4859
Pr_2AuP_2O	1503.6(4)	422.77(8)	993.0(2)	130.88(2)	0.4773
Nd_2AuP_2O	1501.87(5)	420.85(5)	990.3(3)	131.12(1)	0.4715

[a]Data from ref 23.

EXPERIMENTAL SECTION

Synthesis. Starting materials for the ceramic synthesis of RE_2AuP_2O (RE = La−Nd) were ingots of lanthanum (Sigma Aldrich, > 99.9%), cerium (Sigma Aldrich, > 99.9%), praseodymium (Sigma Aldrich, > 99.9%), and neodymium (Koch-Light Lab, > 99.9%); lanthanum(III) oxide (Chempur, > 99.9%), cerium(IV) oxide (Chempur, > 99.99%), praseodymium(III, IV) oxide (Chempur, > 99.9%), and neodymium(III) oxide (ABCR GmbH, > 99.9%), gold (Heraeus, > 99.9%), red phosphorus (Hoechst, ultrapure), sodium chloride (Honeywell, > 99.8%), and potassium chloride, (VWR > 99.8%). Filings of the rare earth elements were prepared from the ingots under dried (sodium) paraffin oil, washed with dried *n*-hexane, and then stored under argon. The argon was purified earlier with titanium sponge (870 K), silica gel, and molecular sieves. Finely dispersed gold was obtained by dissolving gold pieces in *aqua regia* and subsequent precipitation using $(NH_4)_2Fe(SO_4)_2 \cdot xH_2O$ (VWR, > 99%). The filings of the rare earth elements, their appropriate oxides, finely dispersed gold, and powder of red phosphorus were mixed in the ideal molar ratio 1.33:0.33:1:2 (1.5:0.5:1:2 for Ce_2AuP_2O; 1.45:0.55:1:2 for Pr_2AuP_2O). An amount of 0.5 g of the mixture was cold-pressed to a pellet at 100 bar and sealed in an evacuated silica tube. The sample was heated in a resistance furnace to 773 K, held at this temperature for 12 h, and then heated to 873 K, held for 24 h, and finally heated to 1173 K and held for 72 h. The sample was cooled via radiative heat loss by shutting off the furnace. The RE_2AuP_2O samples were obtained as polycrystalline products.

The ceramic synthesis described above did not result in suitable crystals for structure determination. In order to obtain crystals, a salt flux was used. Polycrystalline RE_2AuP_2O (∼200−300 mg) and an equimolar NaCl/KCl mixture (∼1 g) were sealed in evacuated silica tubes. The samples were heated to 1223 K and held at this temperature for 3 days. Subsequently, the ampules were cooled to 873 K at a rate of 2 K h^{-1}, and then to 773 K at a rate of 5 K h^{-1}, and finally to room temperature at a rate of 10 K h^{-1}. Small pillar shaped crystals were isolated from the reaction mixtures by dissolving the NaCl/KCl flux with demineralized water.

The RE_2AuP_2O crystals show dark red to violet surface colors, and at first sight, the edges seem transparent. However, the inner parts of broken crystals clearly show metallic luster.

X-ray Powder Diffraction. The purity of the RE_2AuP_2O powder samples was checked by X-ray powder diffraction in a Guinier camera using Cu $K\alpha_1$ radiation (λ = 154.056 pm) and α-quartz (a = 491.30, c = 540.46 pm) as an internal standard. The Guinier camera was equipped with an image plate system (Fujifilm, BAS−1800). The monoclinic lattice parameters (Table 1) were refined from the powder data by a standard least-squares technique. Proper indexing was ensured by intensity calculations.[24]

Single Crystal X-ray Diffraction. Suitable single crystals of Ce_2AuP_2O, Pr_2AuP_2O, and Nd_2AuP_2O were selected from the samples prepared in the salt fluxes. They were glued to small quartz fibers using bees wax and then examined on a Buerger precession camera (equipped with an image plate system, Fujifilm, BAS-1800) in order to establish the quality for intensity data collection. Single crystal scattering intensity data of Ce_2AuP_2O and Pr_2AuP_2O were collected at room temperature by use of a Stoe IPDS II diffractometer (graphite monochromated Mo Kα radiation) in oscillation mode. A numerical absorption correction was applied to the data set. The Nd_2AuP_2O crystal was measured on a Stoe Stadi Vari diffractometer equipped with a Mo microfocus source and a Pilatus detection system. All relevant crystallographic data and details of the data collection and evaluation are listed in Table 2.

Table 2. Crystal Data and Structure Refinement for RE_2AuP_2O (RE = Ce, Pr, Nd), Space Group $C2/m$, Z = 4

refined composition	Ce_2AuP_2O	Pr_2AuP_2O	Nd_2AuP_2O
formula mass (g mol^{-1})	555.15	556.73	563.39
unit cell dimensions	Table 1	Table 1	Table 1
calculated density (g cm^{-3})	7.59	7.75	7.94
crystal dimensions (μm)	20 × 20 × 80	10 × 10 × 60	10 × 30 × 40
range in θ	2−34°	2−34°	2−35°
detector distance (mm)	70	70	−
exposure time (min)	12	8	−
ω-range ($\Delta\omega$)	0−180°; 0.7°	0−180°; 0.7°	−
integr. param. A, B, EMS	13.2; 3.2; 0.012	12.4; 3.0; 0.012	−
transm. ratio (max/min)	0.475/0.092	0.715/0.293	−
absorption coeff. (mm^{-1})	49.0	51.3	53.2
F(000)	932	940	948
range in hkl	±23, ± 6, ± 15	±22, ± 6, ± 15	±24, ± 6, ± 15
total no. of reflections	3414	3457	20347
independent reflections	1050 (R_{int} = 0.0522)	1037 (R_{int} = 0.0542)	1143 (R_{int} = 0.1898)
reflections with $I > 2\sigma(I)$	969 (R_{sigma} = 0.0380)	750 (R_{sigma} = 0.0662)	601 (R_{sigma} = 0.1364)
data/parameter	1050/38	1037/37	1143/38
goodness-of-fit on F^2	1.021	0.811	0.739
final R indices	R1 = 0.0209	R1 = 0.0257	R1 = 0.0379
$[I > 2\sigma(I)]$	wR2 = 0.0402	wR2 = 0.0372	wR2 = 0.0813
final R indices (all data)	R1 = 0.0246	R1 = 0.0500	R1 = 0.0869
	wR2 = 0.0410	wR2 = 0.0401	wR2 = 0.0944
extinction parameter	0.0038(1)	−	0.0006(1)
largest diff. peak/hole	2.04/−1.73 e Å^{-3}	2.55/−3.15 e Å^{-3}	3.41/−3.90 e Å^{-3}

EDX Analyses. The single crystals investigated on the diffractometers were studied by EDX using a Zeiss EVO MA10 scanning electron microscope with LaF_3, CeO_2, PrF_3, NdF_3, Au, and GaP as standards for the semiquantitative measurements. The analyses at several points of the crystals were close to the ideal RE:Au:P ratio of 2:1:2. No impurity elements (especially from the salt flux) were observed. The oxygen content could not be determined reliably.

Magnetic Susceptibility Measurements. The susceptibility measurements of La_2AuP_2O, Ce_2AuP_2O, and Pr_2AuP_2O (Nd_2AuP_2O was not obtained as single phase material) were carried out on a Quantum Design Physical Property Measurement System using the VSM option. For the measurements, all powdered samples were packed in polypropylene capsules (26.639 mg for La_2AuP_2O, 21.361 mg for Ce_2AuP_2O, and 26.604 mg for Pr_2AuP_2O) and attached to the

dx.doi.org/10.1021/ic302475u | Inorg. Chem. 2013, 52, 2094−2102

Table 3. Refined Atomic Positions and Displacement Parameters of RE_2AuP_2O (RE = Ce, Pr, Nd)[a]

atom	x	z	U_{11}	U_{22}	U_{33}	U_{13}	U_{eq}[b]
Ce_2AuP_2O							
Ce1	0.13162(3)	0.31105(4)	73(1)	62(1)	74(1)	52(1)	67(1)
Ce2	0.17243(3)	0.73151(4)	74(1)	73(1)	67(1)	52(1)	67(1)
Au	0.41128(2)	0.12432(3)	93(1)	82(1)	88(1)	53(1)	92(1)
P1	0.14855(13)	0.0277(2)	132(7)	60(6)	77(6)	66(6)	92(3)
P2	0.54815(13)	0.4517(2)	81(6)	132(7)	76(6)	53(6)	95(3)
O	0.2784(4)	0.6304(6)	95(18)	70(17)	88(17)	62(16)	83(7)
Pr_2AuP_2O							
Pr1	0.13209(5)	0.31171(7)	75(2)	62(3)	70(2)	46(2)	70(1)
Pr2	0.17322(5)	0.73176(7)	76(2)	75(3)	62(2)	44(2)	72(1)
Au	0.41170(4)	0.12524(5)	96(2)	84(2)	79(2)	46(2)	95(1)
P1	0.1487(2)	0.0285(3)	117(11)	79(11)	54(10)	41(9)	95(4)
P2	0.5495(3)	0.4530(4)	132(13)	150(14)	92(11)	78(11)	121(5)
O	0.2770(6)	0.6299(9)	79(29)	59(32)	75(28)	65(25)	61(12)
Nd_2AuP_2O							
Nd1	0.13227(10)	0.31255(15)	148(5)	187(6)	107(5)	93(4)	140(3)
Nd2	0.17372(10)	0.73142(15)	141(5)	215(7)	110(5)	89(4)	150(3)
Au	0.41175(8)	0.12600(11)	157(4)	223(5)	122(4)	85(3)	172(2)
P1	0.1488(5)	0.0292(7)	194(23)	172(26)	101(20)	102(19)	151(9)
P2	0.5492(5)	0.4530(8)	154(24)	209(30)	113(22)	97(21)	152(10)
O	0.2800(14)	0.631(2)	216(69)	193(82)	168(67)	167(61)	160(29)

[a]All atoms lie on Wyckoff Positions 4i (x 0 z). $U_{12} = U_{23} = 0$. [b]U_{eq} is defined as one-third of the derivative of the orthogonalized U_{ij}-tensor. The exponent of the anisotropic displacement parameters is defined through $\exp\{-2\pi^2 \cdot (U_{11}h^2a^{*2} + ... + U_{12}hka^*b^*)\}$.

sample holder rod. The measurements were performed in the temperature range of 3−305 K with magnetic flux densities up to 80 kOe.

^{31}P Solid State NMR. ^{31}P solid state NMR spectra of La_2AuP_2O were recorded at 161.9 MHz on a Bruker Avance DSX 400 spectrometer equipped with 2.5 mm and 4 mm MAS NMR probes. Single-pulse spectra were obtained with 90° pulses of 2.7−4.9 μs length and relaxation delays of 10−80 s using rotor frequencies of 12.0−25.0 kHz. Magnetic shielding anisotropy data were extracted from spectra recorded at low spinning speeds (12.0 kHz), using the DMFIT software (version 2011).[25] The differentiation between the isolated P^{3-} units and P_2^{4-} dumbbells was accomplished by double-quantum (DQ) filtration, based on the excitation of DQ coherences via recoupling of the strong ^{31}P−^{31}P magnetic dipole−dipole interactions present in the dumbbells. To this end, the back-to-back (BABA-xy16) pulse sequence[26,27] was used, applying pairs of 90° pulses of 2.7 μs length for excitation at a MAS spinning speed of 25.0 kHz. The rate of the double quantum coherence buildup was monitored using variable excitation periods ranging from 0.32 to 1.60 ms. All spectra were acquired with an evolution time of 40 μs and a relaxation delay of 60 s. The DQ intensities were normalized to a reference signal that was acquired without an ±180° alternation of the receiver phases as outlined in ref 27. The ^{31}P MAS NMR spectra of Ce_2AuP_2O and Pr_2AuP_2O (both samples were mixed with SiO_2 in a 1:1 mass ratio prior to the measurements) were recorded at 81.0 MHz on a Bruker DSX spectrometer at a spinning frequency of 24.0 kHz. Data were acquired using a rotor synchronized Hahn spin echo with the following experimental parameters: 180° pulse length 3.0 μs, interpulse delay 41.7 μs (one rotor period), relaxation delay 0.1 s. Chemical shifts are reported relative to 85% H_3PO_4.

The ^{139}La NMR spectrum was acquired at 70.65 MHz on an 11.74 T magnet under static conditions and referenced to 1 M $LaCl_3$ solution using the Quadrupolar Carr Purcell Meiboom Gill (QCPMG) sequence.[28,29] In this sequence, defined by the timing scheme $90°-\tau_1-180°-\tau_2-\tau-[\tau_3-180°-\tau_4-2\tau-]_n$, the full Hahn spin echo train, consisting of maxima spaced at $2n\tau$, is being acquired and subsequently Fourier transformed. The intensity distribution of the resulting "spikelet pattern" defines the contours of the static spectrum. For recording these spin echo trains, 90° and 180° pulses of 1.5 and 3.0 μs length, respectively, were used. The pulse separation between the first two pulses (τ_1) and the receiver blanking delays τ_2, τ_3, and τ_4 were all set to 100 μs. The acquisition time for each echo (2τ) was chosen as 200 μs, and n = 40 echoes were acquired in each scan. As the excitation profile obtained under these conditions is narrower than the frequency range covered by the static spectrum, the latter was constituted by co-adding subspectra obtained under systematic stepping of the transmitter frequency in increments of approximately 2700 ppm. Each of these subspectra was the result of 5768 scans, acquired with a recycle delay of 1 s.

Theoretical electric field gradient calculations were conducted using the WIEN2k code.[30] This code is a full-potential all electron method based on the LAPW + LO method and has proven very suitable for calculating the electric field gradient properties of intermetallic compounds. SCF calculations were done with R_{mt} parameters of 2.34 au for La, 2.05 au for P, 2.08 au for O, and 2.37 au for Au. Separation energies between the core and valence states were set to −6.0 Ry. The plane wave cutoff parameter $R_{mt}^{min} \times K_{max}$ was 7.00. For describing the first Brillouin zone, 50−500 k-points were used, yielding comparable results.

Computational Details. Self-consistent DFT band structure calculations were performed using the LMTO-method in its scalar−relativistic version (program TB-LMTO-ASA).[31,32] Reciprocal space integrations were performed with the tetrahedron method using 554 irreducible k-points out of 2048 (grid of 16 × 16 × 8) in the monoclinic Brillouin zone. The basis set consisted of La-6s/{6p}/5d/4f, Au-6s/6p/5d/{4f}, P-3s/3p/{3d}, and O-{3s}/2p/{3d}. Orbitals given in parentheses were downfolded. In order to achieve space filling within the atomic sphere approximation, interstitial spheres are introduced to avoid too large overlap of the atom-centered spheres. The COHP (crystal orbital Hamilton population)[33] method was used for the bond analysis.

RESULTS AND DISCUSSION

Structure Refinements. Systematic analyses of the Ce_2AuP_2O, Pr_2AuP_2O, and Nd_2AuP_2O data set revealed C-centered monoclinic lattices and no further systematic extinctions, in agreement with the centrosymmetric space group $C2/m$, similar to isotypic La_2AuP_2O.[23] The positional parameters of the lanthanum compound were taken as starting

dx.doi.org/10.1021/ic302475u | Inorg. Chem. 2013, 52, 2094−2102

values, and the three structures were refined with anisotropic displacement parameters for all sites using the SHELXL−97 code (full-matrix least-squares on F^2).[34] Refinement of the occupancy parameters revealed no deviations from the ideal compositions. A final difference electron-density map did not reveal any significant residual peaks. The results of the structure refinement are summarized in Table 2. The atomic coordinates and the interatomic distances are listed in Tables 3 and 4.

Table 4. Interatomic Distances (pm) of Ce_2AuP_2O[a]

Ce1:	2	O	238.0(2)	Au:	2	P1	241.5(1)
	1	O	241.6(5)		1	P2	247.4(2)
	1	P1	300.5(2)		1	Ce2	314.7(1)
	2	P2	322.6(1)		2	Ce2	325.3(1)
	1	P1	326.5(2)		2	Ce1	331.3(1)
	2	Au	331.3(1)	P1:	2	Au	241.5(1)
	2	Ce1	372.8(1)		1	Ce1	300.5(2)
	1	P2	375.5(2)		2	Ce2	301.8(1)
	1	Ce2	382.5(1)		1	Ce2	320.8(2)
	2	Ce2	389.3(1)		1	Ce1	326.5(2)
Ce2:	1	O	239.3(4)	P2:	1	P2	221.5(3)
	2	P2	299.6(1)		1	Au	247.4(2)
	2	P1	301.8(1)		2	Ce2	299.6(1)
	1	Au	314.7(1)		2	Ce1	322.6(1)
	1	P1	320.8(2)		2	Ce2	331.9(1)
	2	Au	325.3(1)		1	Ce1	375.5(2)
	2	P2	331.9(1)	O:	2	Ce1	238.0(2)
	1	Ce1	382.5(1)		1	Ce2	239.3(4)
	2	Ce1	389.3(1)		1	Ce1	241.6(5)

[a]All distances within the first coordination spheres are listed. Standard deviations are given in parentheses.

Further information on the structure refinements is available. [Details may be obtained from Fachinformationszentrum Karlsruhe, D-76344 Eggenstein-Leopoldshafen (Germany), by quoting the Registry Nos. CSD−425401 (Ce_2AuP_2O), CSD−425402 (Pr_2AuP_2O), and CSD−425403 (Nd_2AuP_2O).]

Crystal Chemistry. The quaternary phosphide oxides RE_2AuP_2O (*RE* = Ce, Pr, Nd) crystallize with the recently discovered structure type La_2AuP_2O.[23] The cell parameters within the RE_2AuP_2O series decrease from the lanthanum to the neodymium compound as expected from the lanthanoid contraction. The cerium compound nicely fits in between La_2AuP_2O and Pr_2AuP_2O, indicating stable trivalent cerium, in agreement with the magnetic data (vide infra).

In the following, we exemplarily discuss the Ce_2AuP_2O structure. The latter is composed of two characteristic building units. The oxide anions are located in cerium tetrahedra which are *cis*-edge-shared, leading to a chain-like $[Ce_2O]^{4+}$ polycationic unit. These chains are arranged in the form of a distorted hexagonal rod packing (Figure 1). The space between these rods is filled by the $[AuP_2]^{4-}$ polyanions (Figure 2). These are the typical building units in pnictide oxide crystal chemistry; however, the RE_2AuP_2O phases are rare examples for structures where the polycationic and anionic units are arranged in the form of chains and strands and not as layers.

The Ce_2AuP_2O structure contains two crystallographically independent phosphorus sites. The P1 atoms are isolated (i.e., no P−P bonding). They have coordination number (CN) 7 with five cerium and two gold atoms in their coordination shell. The P2 atoms form dumbbells with 222 pm P2−P2, in good agreement with the average P−P single-bond distance of 223 pm.[35] Besides the P2 neighbor, each P2 atoms has seven cerium and one gold neighbors (Figure 3), leading to CN 9 in the form of a tricapped trigonal prism, the typical phosphorus coordination in many metal phosphides.

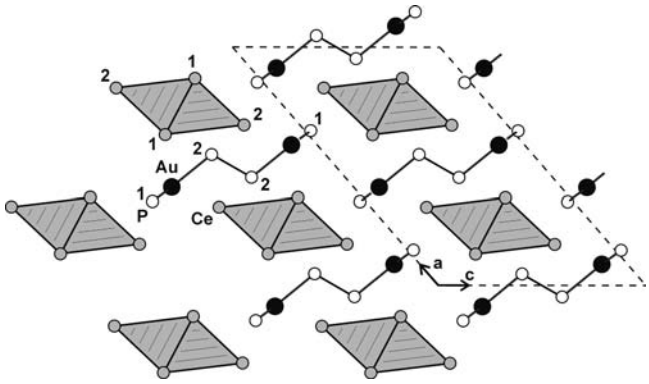

Figure 1. View of the Ce_2AuP_2O structure along the *b* axis. Cerium, gold, and phosphorus atoms are drawn as gray, black-filled, and open circles, respectively. The polycationic chains of *cis*-edge-sharing $[OCe_{4/2}]^{4+}$ tetrahedra and the strands of the $[AuP_2]^{4-}$ polyanion are emphasized.

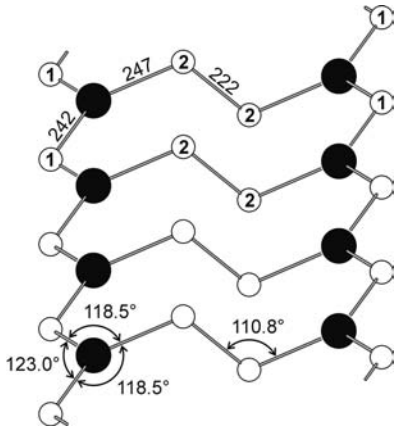

Figure 2. Cutout from the $[AuP_2]^{4-}$ polyanionic building unit in Ce_2AuP_2O. Gold and phosphorus atoms are drawn as black-filled circles and open circles, respectively. Relevant interatomic distances (pm), bond angles (deg), and atom designations are given.

Ce_2AuP_2O is an electron-precise phosphide oxide. On the basis of the magnetic susceptibility data (vide infra), the cerium atoms are trivalent. Ce(1) has nine directly coordinated neighbors (three O, four P, and 2 Au atoms), while Ce(2) is eleven-coordinated by one O, three Au and seven P atoms. The

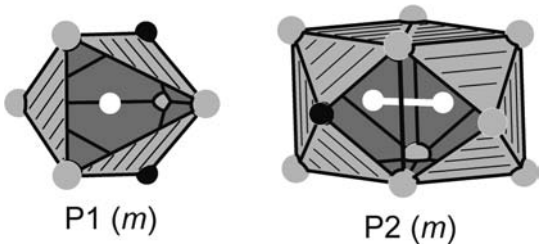

Figure 3. Coordination polyhedra of the phosphorus atoms in Ce_2AuP_2O. Lanthanum, gold, and phosphorus atoms are drawn as gray, black, and white circles, respectively. The site symmetries are given.

dx.doi.org/10.1021/ic302475u | Inorg. Chem. 2013, 52, 2094−2102

Au atoms have approximately trigonal planar phosphorus coordination, which is typical for Au(I). The isolated phosphorus atoms can be considered as phosphide anions $P1^{3-}$ and $(P2-P2)^{4-}$dumbbells. For two formula units, we then obtain $(4Ce^{3+})(2Au^{+})(2P^{3-})(P_2^{4-})(2O^{2-})$.

Electronic Structure of La_2AuP_2O. Band structure calculations were conducted using the TB-LMTO method. The total density of states (DOS) is shown in Figure 4. The La-

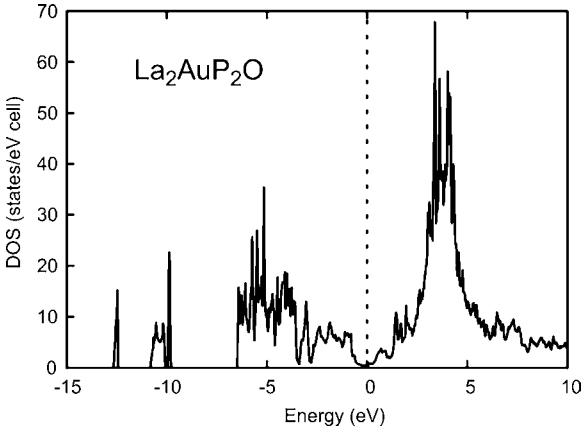

Figure 4. Electronic density of states of La_2AuP_2O. Energy zero is taken at the Fermi level.

4*f* states are well above the Fermi energy (+4 eV) as expected for La^{3+}. The DOS exhibits a minimum at the Fermi level, but no energy gap is discernible. The contributions of the atomic orbitals to the DOS at the Fermi level are roughly 28% La, 28% P, 17% Au, 11% O, and 16% empty spheres. This metallic state of La_2AuP_2O is in agreement with the metallic luster of the crystals and the magnetic data. The Au-5*d* states between −5 and −7 eV are occupied and overlap with the P-3*p* states. The COHP analysis of the Au−P and P−P bonds reveal fully occupied bonding states and nonbonding character at the Fermi energy, respectively. These results are consistent with the charge balanced formula splitting $(La^{3+})_2Au^{+}P^{3-}P^{2-}O^{2-}$ in spite of the metallic properties.

^{31}P Solid State NMR. Figure 5 shows the fast- and slow-spinning ^{31}P MAS NMR spectra of La_2AuP_2O and the corresponding simulations; the latter resulting in the chemical shift tensor parameters listed in Table 5. The isolated P1 and dumbbell P2 atoms are observed in the exact 1:1 ratio expected from the crystal structure. The small isotropic magnetic shift

Table 5. ^{31}P Chemical Shielding Anisotropy Parameters of La_2AuP_2O Using the Following Convention: $\Delta\sigma = \sigma_{zz} - 1/2(\sigma_{xx} + \sigma_{yy})$ and $\eta_\sigma = (\sigma_{yy} - \sigma_{xx})/(\sigma_{zz} - \sigma_{iso})$ and $|\sigma_{zz} - \sigma_{iso}| > |\sigma_{xx} - \sigma_{iso}| > |\sigma_{yy} - \sigma_{iso}|$

	δ_{iso} (ppm)	$\lvert\Delta\sigma\rvert$ (ppm)	η_σ
P1	239.0	269.0	0.85
P2	−95.4	226.3	0.4

values relative to the 85% H_3PO_4 standard indicate the absence of Knight shifts that are typically observed in metallic compounds, and the peak separation between the two resonances (239 and −95 ppm) is interpreted as a difference in isotropic chemical shifts arising from the different types of phosphorus coordination environments. There is also a substantial difference in the asymmetry parameters of the anisotropic magnetic shielding tensors characterizing these sites (Table 5). Both signals are characterized by short spin−lattice relaxation times (near 8 s), consistent with the semimetallic character of this compound. An unambiguous assignment is possible by means of recoupling the strong ^{31}P−^{31}P magnetic dipole dipole couplings within the P_2^{4-} dumbbells. Figure 6a compares the reference ^{31}P MAS NMR spectrum with that obtained using ^{31}P double-quantum filtering applying the standard back-to-back (BABA-xy16) pulse sequence, with an excitation length of 640 μs. This spectrum is clearly dominated by the signal at −95 ppm, which therefore has to be assigned to the dumbbell species. This assignment is confirmed by systematic measurements of the single-quantum-detected intensity of the DQ coherence as a function of excitation time (Figure 6b), revealing a much faster buildup for this signal as compared to the 239 ppm signal. The sharp resonance near 0 ppm is assigned to an oxide impurity. Figure 7 shows the room temperature ^{31}P MAS NMR spectra of the cerium and the praseodymium compounds. The spectra are dominated by nuclear-electron magnetic hyperfine interactions, with strong isotropic and anisotropic components. The isotropic component is responsible for MAS center bands that are strongly paramagnetically shifted, while the anisotropic component results in significant inhomogeneous line broadening producing wide spinning sideband patterns for these signals under MAS conditions. In the case of Ce_2AuP_2O, two distinct resonances centered at 1935 and 893 ppm are observed in a 1:1 ratio, consistent with the crystallographic information. Attempts to assign these resonances based on the BABA experiment described above were unsuccessful, presumably because of the

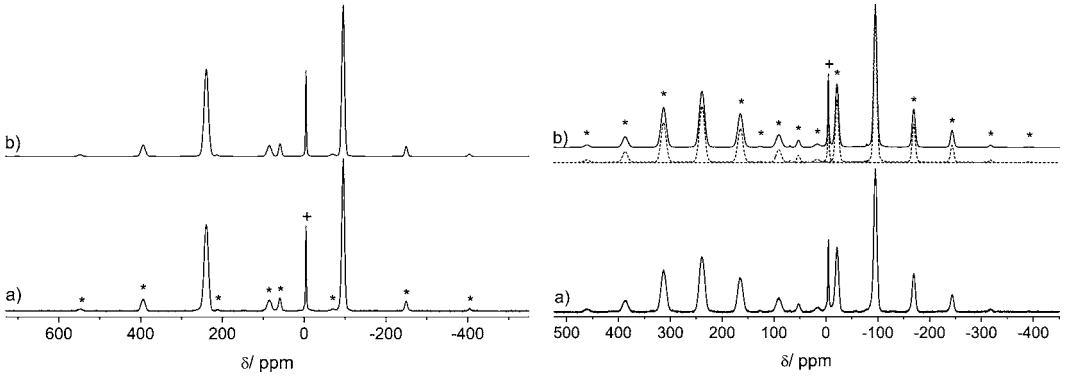

Figure 5. Experimental (a) and simulated (b) ^{31}P MAS NMR spectrum of La_2AuP_2O. Left side: spinning frequency 25.0 kHz. Right side: spinning frequency 12.0 kHz. + marks an impurity. Symbol ∗ indicates spinning sidebands.

dx.doi.org/10.1021/ic302475u | Inorg. Chem. 2013, 52, 2094−2102

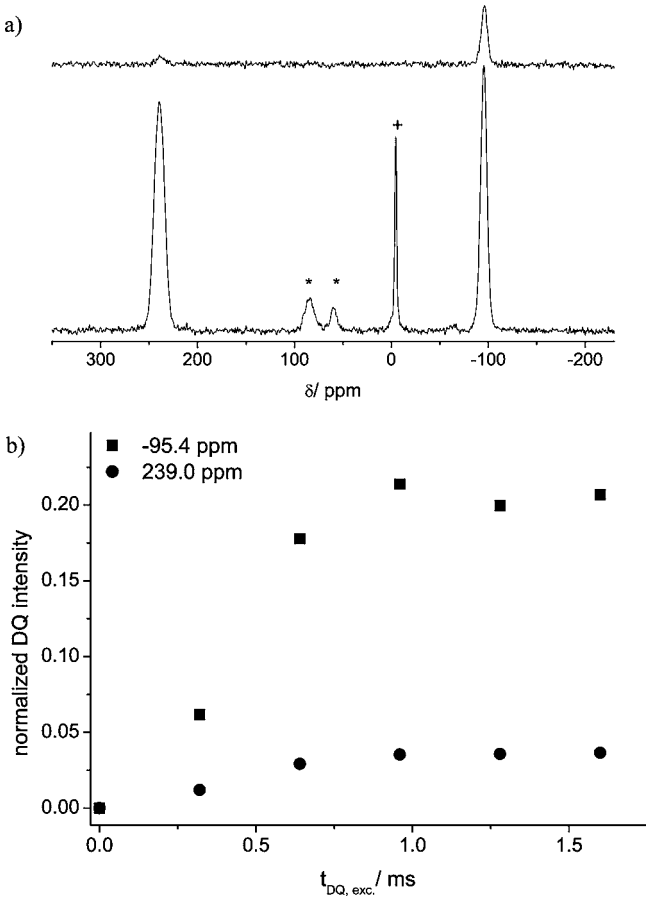

Figure 6. (a) ^{31}P MAS NMR spectrum measured at 161.9 MHz and a spinning frequency of 25 kHz without (bottom) and with double-quantum filtration (top). Symbols ∗ mark spinning sidebands and + an impurity. (b) Dependence of the ^{31}P double-quantum coherence intensity on excitation time for the two resonances in La_2AuP_2O.

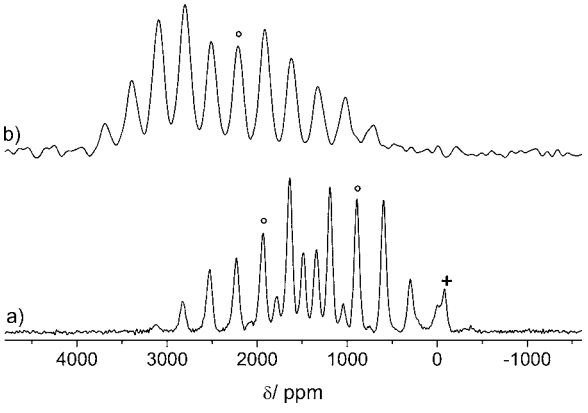

Figure 7. ^{31}P MAS NMR spectra of (a) Ce_2AuP_2O and (b) Pr_2AuP_2O acquired at 4.7 T with a rotation frequency of 24 kHz. Circles indicate the isotropic MAS center bands. Symbol + marks an impurity.

fast spin−lattice and spin−spin relaxation times of this compound. In the case of Pr_2AuP_2O, only one broad MAS peak pattern centered near 2200 ± 10 ppm and extending over an even wider frequency range could be detected. In this case, the extremely strong paramagnetic broadening makes it impossible to resolve the two distinct signals expected from the crystal structure. The stronger magnetic hyperfine interaction evident for this compound is consistent with the larger magnetic moment of Pr^{3+} compared to Ce^{3+} as also evident from the magnetic susceptibility data discussed below.

^{139}La NMR. Figure 8 shows the spikelet pattern arising from the Fourier transformation of the QCPMG spin echo train. The

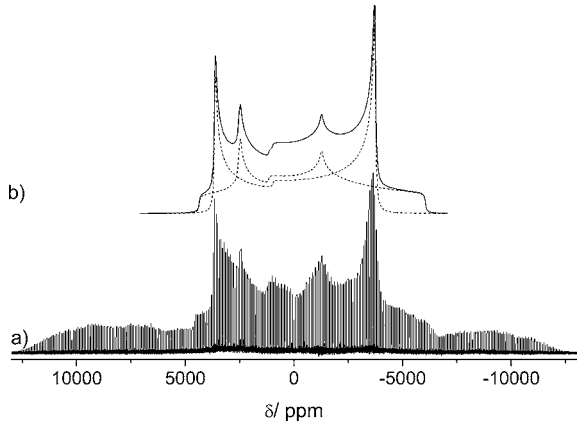

Figure 8. (a) Static ^{139}La NMR spectrum of La_2AuP_2O at70.65 MHz. (b) Simulated spectrum in terms of two distinct spectral contributions with an area ratio of 1:1.

spikelets map the envelope of the central $m = 1/2 \leftrightarrow -1/2$ transition of the ^{139}La static NMR spectrum; in addition, part of the satellite transition patterns are visible, both at the high- and low-frequency end of the spectral window. The line shape of the central transition envelope is dominated by nuclear electric quadrupolar interactions. For the simulation, second-order perturbation theory was found to be sufficient, and contributions arising from anisotropic magnetic shielding were neglected. On the basis of these assumptions, we found it possible to simulate the spectrum in terms of two superimposed second-order powder patterns in a 1:1 ratio, consistent with the crystal structure. Table 6 summarizes the

Table 6. ^{139}La Isotropic Magnetic Shifts δ_{ms}^{iso}, Nuclear Electric Quadrupole Coupling Constants C_Q, and Electric Field Gradient Asymmetry Parameters η_Q of La_2AuP_2O[a]

Site	δ_{ms}^{iso}(±10 ppm)	C_Q(±0.5 MHz)	η_Q(±0.05)
La(1)	843	51.5 (52.0)	0.53 (0.67)
La(2)	983	52.6 (51.6)	0.00 (0.01)

[a]Values in parentheses are calculated using the WIEN2k code.

corresponding interaction parameters, isotropic magnetic shift values δ_{ms}^{iso}, nuclear electric quadrupolar coupling constants C_Q, and electric field gradient asymmetry parameters η_Q. The large magnitude of the nuclear electric quadrupolar coupling constant is comparable to that measured in other asymmetrically coordinated La compounds that have been recently measured using the QCPMG method.[36−38] Comparison of the C_Q and η_Q values with theoretical values calculated with the WIEN2k code allows an unambiguous assignment of La(1) and La(2). It is interesting to note that even though the crystallographic point symmetries of both La sites are identical, the differences in the local O/P coordinations result in significant differences in the electric field gradient asymmetry parameter. While the value is close to zero for La in the phosphorus-dominated environment, the η_Q-value for the La site in the oxygen-dominated environments lies in the vicinity of 0.5−0.6. Finally, the simulation also results in values of the

dx.doi.org/10.1021/ic302475u | Inorg. Chem. 2013, 52, 2094−2102

isotropic relative magnetic shifts δ_{ms}^{iso}. These comprise contributions from a local term ("chemical shift") and a term arising from the nuclear spin interactions with unpaired spin density associated with the conduction electrons ("Knight shift"). These two contributions cannot be separated, and only the combined magnetic shielding interaction is measured. For both La sites, the large positive δ_{ms}^{iso} values suggest that the Knight shift contributions are substantial. This is not unexpected considering that the La atoms make significant contributions to the density of states in the vicinity of the Fermi level (see above).

Magnetic Susceptibility Data. The temperature dependence of the magnetic susceptibility of La_2AuP_2O is shown in Figure 9. The magnetic susceptibility has a negative value above

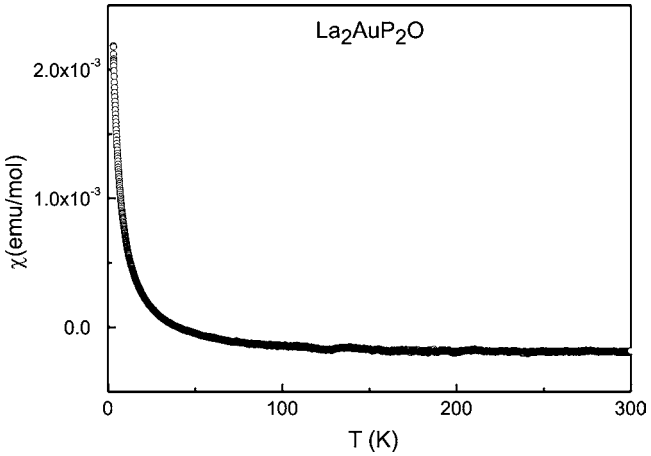

Figure 9. Temperature dependence of the magnetic susceptibility of La_2AuP_2O measured at an external field strength of 10 kOe.

40 K and is nearly temperature independent above 100 K. At 300 K, the value is -1.9×10^{-4} emu mol^{-1}. This is typical behavior for a diamagnetic compound, and the slight upturn of the magnetic susceptibility (Curie tail) below 50 K can be attributed to minor paramagnetic impurities in the sample. The core diamagnetism overcompensates the small Pauli contribution.

The top panel of Figure 10 displays the temperature dependence of the magnetic and inverse magnetic susceptibility (χ and χ^{-1} data) of Ce_2AuP_2O measured at 10 kOe. A fit of the χ^{-1} data in the region of 50−300 K using the Curie−Weiss law, revealed an effective magnetic moment of $\mu_{eff} = 2.35(1)\ \mu_B$/Ce atom and a Weiss constant of $\theta_p = -5.3(1)$ K. The negative value of the Weiss constant points toward weak antiferromagnetic interactions in the paramagnetic range. The effective magnetic moment is somewhat smaller than the theoretical value of 2.54 μ_B for a free Ce^{3+} ion. However, this deviation has also been observed in other cerium phosphide oxides such as CeZnPO[39] and CeRuPO.[40] The susceptibility data also shows antiferromagnetic ordering at around 10 K.

To obtain more precise information about this ordering, low-field measurements were performed in a zero-field- and field-cooled mode, which are shown in the middle of Figure 10. No bifurcation between the ZFC- and the FC-curves is visible, and the Néel temperature could be determined to $T_N = 13.1(5)$ K.

A tiny anomaly is evident in the Ce_2AuP_2O susceptibility data around 30 K that is due to a trace amount of ferromagnetic Ce_2AuP_3,[41] which is not visible on the Guinier powder pattern.

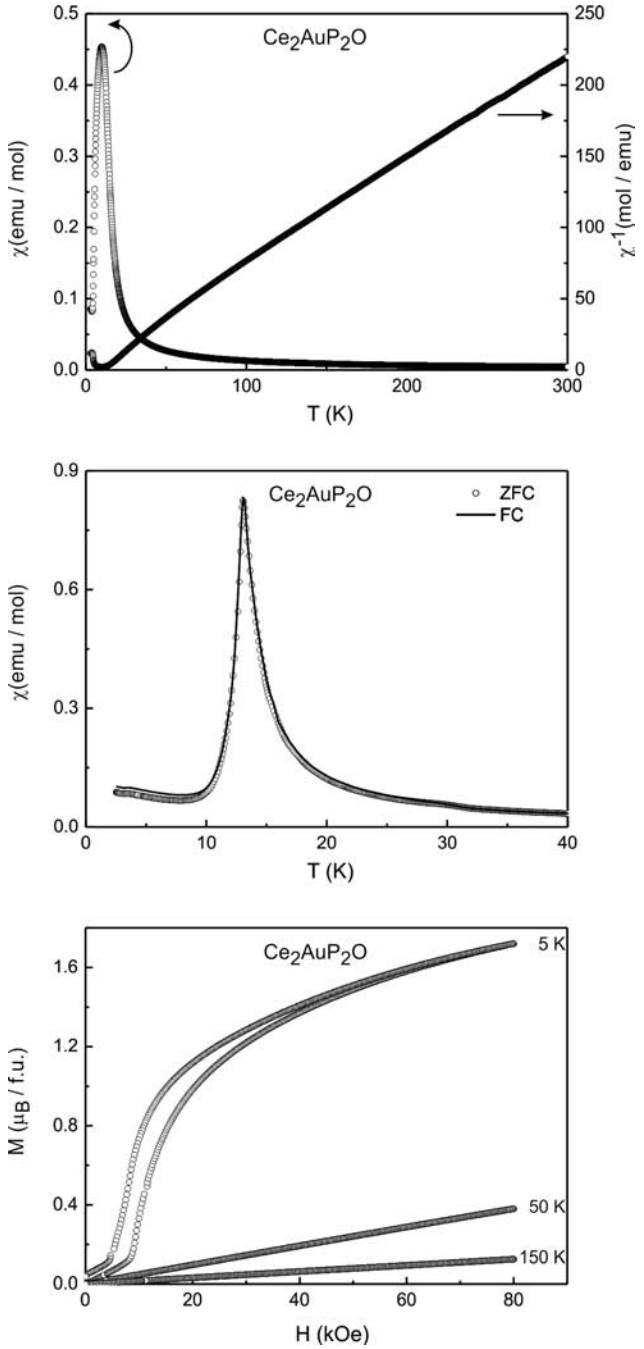

Figure 10. Magnetic properties of Ce_2AuP_2O. (Top) Temperature dependence of the magnetic susceptibility (χ and χ^{-1} data) measured at 10 kOe. (Middle) Magnetic susceptibility in zero-field- and field-cooled mode at 100 Oe. (Bottom) Magnetization isotherms at 5, 50, and 150 K.

This trace also affects the magnetization data and leads to a small residual magnetization when decreasing the field.

The bottom panel in Figure 10 displays the magnetization isotherms of Ce_2AuP_2O measured at 5, 50, and 150 K. The isotherms above the ordering temperature (50 and 150 K) both display a linear field dependency of the magnetization as expected for a paramagnetic material. At 5 K, the magnetization increases linearly at first, followed by a steep increase at a field strength of around 8 kOe. This sharp increase can be attributed to a reorientation of the spins, which confirms the antiferromagnetic ground state. The critical field for the

dx.doi.org/10.1021/ic302475u | Inorg. Chem. 2013, 52, 2094−2102

metamagnetic step can be determined to 11.5(5) kOe. At high fields, a tendency for saturation can be observed, and the magnetic moment at 5 K and 80 kOe (0.86(1) μ_B/Ce atom) is much lower than the expected saturation magnetization of 2.14 μ_B according to $g_J \times J$. Such reduced magnetization values often occur in cerium compounds and can be attributed to crystal field splitting of the $J = 5/2$ magnetic ground state of Ce^{3+}. One peculiarity that should be mentioned is the unusual hysteresis over nearly the entire range of the applied magnetic field.

The top panel of Figure 11 displays the temperature dependence of the magnetic and inverse magnetic susceptibility (χ and χ^{-1} data) of Pr_2AuP_2O measured at 10 kOe. Above 50 K, the χ^{-1} data can be fitted using the Curie–Weiss law resulting in an effective magnetic moment of μ_{eff} = 3.48(1) μ_B/Pr atom, which is in good agreement with the free ion value of 3.58 μ_B for Pr^{3+}. The negative value of θ_p = −9.7(1) K for the Weiss constant indicates weak antiferromagnetic interactions in the paramagnetic range; however, the steep incline of the χ data below 10 K points toward ferromagnetic ordering.

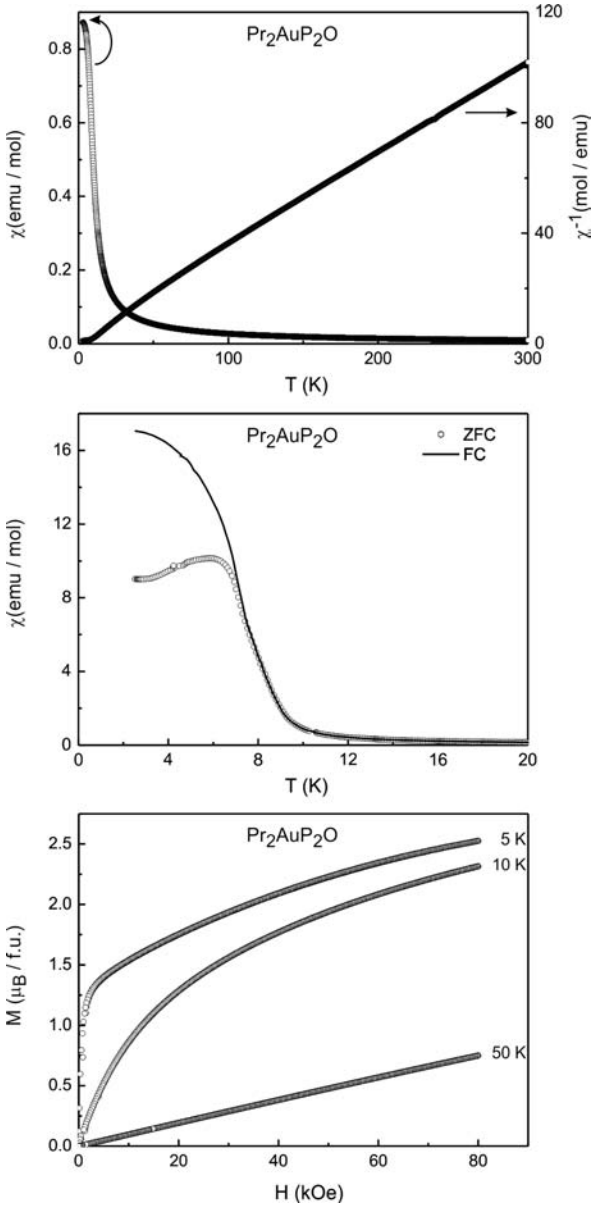

Figure 11. Magnetic properties of Pr_2AuP_2O. (Top) Temperature dependence of the magnetic susceptibility (χ and χ^{-1} data) measured at 10 kOe. (Middle) Magnetic susceptibility in zero-field- and field-cooled mode at 100 Oe. (Bottom) Magnetization isotherms at 5, 10, and 50 K.

To study possible magnetic ordering phenomena, low-field measurements were performed in zero-field- and field-cooled mode as shown in the middle panel of Figure 11. These clearly establish a ferromagnetic ordering, and the Curie temperature can be determined from the minimum of the derivative $d\chi/dT$ to T_C = 7.0(5) K from the FC curve. A ferromagnetic ordering and a negative Weiss constant do not contradict each other because θ_p only indicates which interactions are predominant in the paramagnetic range.

The magnetization isotherms measured at 5, 10, and 50 K are shown in the bottom panel of Figure 11. At 10 K, a slight curvature is observed due to the onset of long-range and/or paramagnetic saturation effects; whereas, at 50 K there is a linear dependence of the magnetization to the applied external field as expected for a paramagnetic material. Corresponding to the results of the kink-point measurement, the magnetization isotherm at 5 K (below T_C) clearly indicates a canted ferromagnetic alignment with a sharp increase at low applied fields and a tendency for saturation at higher fields. The magnetic moment at 5 K and 80 kOe (1.27(1) μ_B/Pr atom) is much lower than the expected saturation magnetization of 3.20 μ_B according to $g_J \times J$. As observed for the cerium compounds, this is most likely caused by crystal-field splitting of the $J = 4$ magnetic ground state for Pr^{3+}. However, it can be noticed that full saturation at this field strength has also not yet completely set in. Over the entire magnetic field range, no hysteresis can be observed.

CONCLUSIONS

New electron-precise quaternary phosphide oxides RE_2AuP_2O (RE = Ce, Pr, Nd) contain one-dimensional polycationic and anionic building units $[RE_2O]^{4+}$ and $[AuP_2]^{4-}$ with P^{3-} and P_2^{4-} entities in the polyanion. In the isostructural lanthanum compound, the crystallographically distinct phosphorus species can clearly be distinguished by ^{31}P solid state NMR spectroscopy and assigned based on advanced dipolar NMR methods. Likewise, the crystallographically distinct lanthanum species can be differentiated and assigned on the basis of the ^{139}La electric field gradient asymmetry parameter, as measured by ^{139}La NMR. The rare earth atoms are in a stable trivalent state, and magnetic ordering is detected for the cerium and praseodymium magnetic moments at 13.1 and 7.0 K, respectively.

ASSOCIATED CONTENT

Supporting Information

Crystallographic data in CIF format. This material is available free of charge via the Internet at http://pubs.acs.org.

AUTHOR INFORMATION

Corresponding Author

*E-mail: pottgen@uni-muenster.de.

Notes

The authors declare no competing financial interest.

ACKNOWLEDGMENTS

We thank Dipl.-Ing. U. Ch. Rodewald for the intensity data collections. This work was supported by the Deutsche

Forschungsgemeinschaft through SPP 1458 *Hochtemperatursupraleitung in Eisenpnictiden*. O.N. and T.W. thank the NRW Forschungsschule *Molecules and Materials – A Common Design Principle* for doctoral fellowships. T.W. also acknowledges support from the Fonds der Chemischen Industrie for a two-year doctoral stipend.

REFERENCES

(1) Pfisterer, M.; Nagorsen, G. *Z. Naturforsch.* **1980**, *35b*, 703–704.
(2) Rotter, M.; Tegel, M.; Johrendt, D.; Schellenberg, I.; Hermes, W.; Pöttgen, R. *Phys. Rev. B* **2008**, *78*, 020503.
(3) Rotter, M.; Tegel, M.; Johrendt, D. *Phys. Rev. Lett.* **2008**, *101*, 107006.
(4) Quebe, P.; Terbüchte, L. J.; Jeitschko, W. *J. Alloys Compd.* **2000**, *302*, 70–74.
(5) Kamihara, Y.; Watanabe, T.; Hirano, M.; Hosono, H. *J. Am. Chem. Soc.* **2008**, *130*, 3296–3297.
(6) Brock, S. L.; Kauzlarich, S. M. *Comments Inorg. Chem.* **1995**, *17*, 213–238.
(7) Pöttgen, R.; Johrendt, D. *Z. Naturforsch.* **2008**, *63b*, 1135–1148.
(8) Johrendt, D.; Pöttgen, R. *Angew. Chem.* **2008**, *120*, 4860–4863; *Angew. Chem., Int. Ed.* **2008**, *47*, 4782–4784.
(9) Ozawa, T. C.; Kauzlarich, S. M. *Sci. Technol. Adv. Mater.* **2008**, *9*, 033003.
(10) Wen, H.-H. *Adv. Mater.* **2008**, *20*, 3764–3769.
(11) Sadovskii, M. V. *Phys.–Usp.* **2008**, *51*, 1201–1227.
(12) Ivanovski, A. L. *Phys.–Usp.* **2008**, *51*, 1229–1260.
(13) Izyumov, Yu. A.; Kurmaev, E. Z. *Phys. Usp.* **2008**, *51*, 11261–1286.
(14) Clarke, S. J.; Adamson, P.; Herkelrath, S. J. C.; Rutt, O. J.; Parker, D. R.; Pitcher, M. J.; Smura, C. F. *Inorg. Chem.* **2008**, *47*, 8473–8486.
(15) Hosono, H. *J. Phys. Soc. Jpn. Suppl. C* **2008**, *77*, 1–8.
(16) Ishida, K.; Nakai, Y.; Hosono, H. *J. Phys. Soc. Jpn.* **2009**, *78*, 062001.
(17) Hosono, H.; Ren, Z.-A. *New J. Phys.* **2009**, *11*, 025003.
(18) Chu, P. C. W.; Koshelev, A.; Kwok, W.; Mazin, I.; Welp, U.; Wen, H.-H., Eds.; *Phys. C* **2009**; Vol. *469*, pp 313–674.
(19) Johnston, D. C. *Adv. Phys.* **2010**, *59*, 803–1061.
(20) Johrendt, D.; Hosono, H.; Hoffmann, R.-D.; Pöttgen, R. *Z. Kristallogr.* **2011**, *226*, 435–446.
(21) Johrendt, D. *J. Mater. Chem.* **2011**, *21*, 13726–13736.
(22) Eul, M.; Johrendt, D.; Pöttgen, R. *Z. Naturforsch.* **2009**, *64b*, 1352–1359.
(23) Eul, M.; Möller, M. H.; Hoffmann, R.-D.; Jeitschko, W.; Pöttgen, R. *Z. Anorg. Allg. Chem.* **2012**, *638*, 331–335.
(24) Yvon, K.; Jeitschko, W.; Parthé, E. *J. Appl. Crystallogr.* **1977**, *10*, 73–74.
(25) Massiot, D.; Fayon, F.; Capron, M.; King, I.; Le Calve, S.; Alonso, B.; Durand, J. O.; Bujoli, B.; Gan, Z.; Hoatson, G. *Magn. Reson. Chem.* **2002**, *40*, 70–76.
(26) Feike, M.; Demco, D. E.; Graf, R.; Gottwald, J.; Hafner, S.; Spiess, H. W. *J. Magn. Reson., Ser. A* **1996**, *122*, 214–221.
(27) Saalwächter, K.; Lange, F.; Matyjaszewski, K.; Huang, C.-F.; Graf, R. *J. Magn. Reson.* **2011**, *212*, 204–215.
(28) Larsen, F. H.; Jakobsen, H. J.; Ellis, P. D.; Nielsen, N. C. *J. Phys. Chem. A* **1997**, *101*, 8597.
(29) Siegel, R.; Nakashima, T. T.; Wasylishen, R. E. *J. Phys. Chem. B* **2004**, *108*, 2218.
(30) Blaha, P.; Schwarz, K.; Madsen, G. K. H.; Kvasnicka, D.; Luitz, J. *WIEN2k, An Augmented Plane Wave + Local Orbitals Program for Calculateing Crystal Properties*; Schwarz, K. H., Ed.; Technical University Wien: Austria, 2001.
(31) Andersen, O. K.; Jepsen, O. *Tight-Binding LMTO*, Version 47c; Max-Planck-Institut für Festkörperforschung : Stuttgart, 1994.
(32) Andersen, O. K.; Jepsen, O.; Sob, M. Linearized Band Structure Methods. In *Electronic Band Structure and Its Applications, Lecture Notes in Physics*; Yussouff, M., Ed.; Springer Verlag: Berlin, 1987; Vol. *283*, pp 1–57.
(33) Dronskowski, R.; Blöchl, P. E. *J. Phys. Chem.* **1993**, *97*, 8617–24.
(34) (a) Sheldrick, G. M. *SHELXL-97*, Program for Crystal Structure Refinement; University of Göttingen: Germany, 1997. (b) Sheldrick, G. M. *Acta Crystallogr.* **2008**, *A64*, 112–122.
(35) Pöttgen, R.; Hönle, W.; von Schnering, H. G. Phosphides: Solid State Chemistry. In *Encyclopedia of Inorganic Chemistry*, 2nd ed.; King, R. B., Ed.; Wiley: New York, 2005; Vol. *VII*, pp 4255–4308.
(36) Ooms, K. J.; Feindel, K. W.; Willans, M. J.; Wasylishen, R. E.; Hanna, J. V.; Pike, K. J.; Smith, M. E. *Solid State Nucl. Magn. Reson.* **2005**, *28*, 125.
(37) Hamaed, H.; Lo, A. Y. H.; Lee, D. S.; Evans, W. J.; Schurko, R. W. *J. Am. Chem. Soc.* **2006**, *128*, 12638.
(38) Willans, M. J.; Feindel, K. W.; Ooms, K. J.; Wasylishen, R. E. *Chem.—Eur. J.* **2006**, *12*, 159.
(39) Lincke, H.; Glaum, R.; Dittrich, V.; Tegel, M.; Johrendt, D.; Hermes, W.; Möller, M. H.; Nilges, T.; Pöttgen, R. *Z. Anorg. Allg. Chem.* **2008**, *634*, 1339–1348.
(40) Krellner, C.; Kini, N. S.; Brüning, E. M.; Koch, K.; Rosner, H.; Nicklas, M.; Baenitz, M.; Geibel, C. *Phys. Rev. B* **2007**, *76*, 104418.
(41) Eschen, M.; Kotzyba, G.; Künnen, B.; Jeitschko, W. *Z. Anorg. Allg. Chem.* **2001**, *627*, 1699–1708.